

# Monitoring groundwater-surface water interaction using time-series and time-frequency analysis of transient three-dimensional electrical resistivity changes

T. C. Johnson,<sup>1</sup> L. D. Slater,<sup>2</sup> D. Ntarlagiannis,<sup>2</sup> F. D. Day-Lewis,<sup>3</sup> and M. Elwaseif<sup>2</sup>

Received 20 January 2012; revised 3 May 2012; accepted 26 May 2012; published 10 July 2012.

[1] Time-lapse resistivity imaging is increasingly used to monitor hydrologic processes. Compared to conventional hydrologic measurements, surface time-lapse resistivity provides superior spatial coverage in two or three dimensions, potentially high-resolution information in time, and information in the absence of wells. However, interpretation of time-lapse electrical tomograms is complicated by the ever-increasing size and complexity of long-term, three-dimensional (3-D) time series conductivity data sets. Here we use 3-D surface time-lapse electrical imaging to monitor subsurface electrical conductivity variations associated with stage-driven groundwater-surface water interactions along a stretch of the Columbia River adjacent to the Hanford 300 near Richland, Washington, USA. We reduce the resulting 3-D conductivity time series using both time-series and time-frequency analyses to isolate a paleochannel causing enhanced groundwater-surface water interactions. Correlation analysis on the time-lapse imaging results concisely represents enhanced groundwater-surface water interactions within the paleochannel, and provides information concerning groundwater flow velocities. Time-frequency analysis using the Stockwell (S) transform provides additional information by identifying the stage periodicities driving groundwater-surface water interactions due to upstream dam operations, and identifying segments in time-frequency space when these interactions are most active. These results provide new insight into the distribution and timing of river water intrusion into the Hanford 300 Area, which has a governing influence on the behavior of a uranium plume left over from historical nuclear fuel processing operations.

**Citation:** Johnson, T. C., L. D. Slater, D. Ntarlagiannis, F. D. Day-Lewis, and M. Elwaseif (2012), Monitoring groundwater-surface water interaction using time-series and time-frequency analysis of transient three-dimensional electrical resistivity changes, *Water Resour. Res.*, 48, W07506, doi:10.1029/2012WR011893.

## 1. Introduction

[2] Electrical resistivity tomography (ERT) is a promising noninvasive technology for investigating groundwater-surface water exchanges [e.g., Acworth and Dasey, 2003; Mansoor and Slater, 2007; Nyquist et al., 2008; Singha et al., 2008]. Application of the technique is based on monitoring natural contrasts in the electrical conductance of groundwater and surface water [e.g., Henderson et al., 2010], electrical contrasts induced by the addition of tracers to streams [e.g., Ward et al., 2010], or mapping of streambed or aquifer properties based on the static imaging of lithologic variations controlling

exchange [e.g., Crook et al., 2008; Slater et al., 2010]. The major advantage of the method is that information on exchange is not localized at the streambed, but can be imaged beyond the bed. In contrast, other emerging technologies, such as fiber optic-distributed temperature sensing (FO-DTS) commonly only provide information at points along the fiber optic cable, which is deployed on the streambed [Selker et al., 2006].

[3] Opportunities to enhance the information on groundwater-surface water exchange obtainable from ERT have increased with the development of continuous, autonomous resistivity data acquisition systems that can provide temporally rich data sets. Time-lapse ERT is frequently used to infer hydrological processes and to separate out transient changes in resistivity occurring due to the flow of solutes and moisture from static lithological controls on resistivity. The common approach is to reconstruct a time sequence of resistivity, or changes in resistivity from some starting condition, and to interpret changes in the resistivity in terms of solute or moisture dynamics [Kemna et al., 2006]. Hydrological interpretation of time-lapse resistivity inversions can be facilitated by constructing a dense network of resistivity time series that are considered proxies of moisture content or specific conductance variation [e.g., Johnson et al., 2010; Slater et al., 2000, 2002].

<sup>1</sup>Energy and Environment Directorate, Pacific Northwest National Laboratory, Richland, Washington, USA.

<sup>2</sup>Department of Earth and Environmental Sciences, Rutgers University, Newark, New Jersey, USA.

<sup>3</sup>Office of Groundwater, Branch of Geophysics (OGW-BG), U.S. Geological Survey, Storrs, Connecticut, USA.

Corresponding author: T. C. Johnson, Energy and Environment Directorate, Pacific Northwest National Laboratory, 902 Battelle Blvd., PO Box 999, MSIN K9-33, Richland, WA 99352, USA. (tj@pnnl.gov)

[4] Despite the clear potential of resistivity imaging, the increasing capability to rapidly collect time-lapse resistivity measurements requires the development of novel methods for extracting and representing the key hydrological information in such temporally and spatially rich data sets. Three-dimensional (3-D) time-lapse imaging produces extensive databases that are difficult to mine for salient information using simple visualization or exploratory statistics. The visual presentation of time sequences of resistivity, or changes in resistivity, is unlikely to adequately summarize the information content available in such data sets. Time series analysis is a powerful tool to interpret the driving forces that govern temporal variations in environmental parameters. Studying the frequency content of geophysical time series has long proven effective for enhancing the information extracted from geophysical data sets [Binley *et al.*, 1996; de Voogd and den Rooijen, 1983; Sinha *et al.*, 2009]. However, time series analysis has hitherto not been exploited to improve the interpretation of time-lapse ERT images, presumably due to the relatively short time frames and coarse sampling intervals in previous studies. The recent advent of semicontinuous monitoring using short data acquisition times presents opportunities to perform time series analysis on a dense array of elements making up a 3-D time-lapse resistivity inversion. Important hydrological questions in the studies of groundwater-surface water exchange to be addressed using time-lapse resistivity include: What is the spatial extent of groundwater-surface water mixing?; What hydrogeologic conditions determine the spatiotemporal variability in this exchange?; and Where are the preferred flow pathways governing exchange between the river and the aquifer?

[5] The objective of this study was to use 3-D time-lapse ERT imaging to better understand the dynamics of groundwater-surface water exchange at a site where stage variations driven by daily dam operations exert a complex boundary condition on the flow and transport of contaminated groundwater toward a major river corridor. We show how time series analysis of the elements making up a semicontinuous ERT inversion can provide unique insights into the controls of stage variations on the exchange of surface water and groundwater in the saturated portion of an unconfined aquifer, and the localized permeability structure (i.e., a high permeability paleochannel) that governs that exchange. The results illustrate that this treatment of time-lapse ERT captures unique hydrological information at spatiotemporal scales unobtainable using invasive hydrological measurement methods.

## 2. Study Site

[6] For more than 40 yrs, starting in 1943, fluids containing radioisotopes and metals generated during reactor fuel fabrication and chemical separation processes were discharged to the shallow subsurface of the U. S. Department of Energy (DOE) Hanford 300 Area, Richland, Washington (Figure 1). The primary chemical inventories included 241 t of copper, 117 t of fluorine, 2060 t of nitrate, and between 33 and 59 t of uranium (U), which is currently the primary contaminant of concern. A 1993 modeling study predicted that groundwater U concentrations would decrease to the  $30 \mu\text{g L}^{-1}$  drinking-water standard in 3–10 yrs [Westinghouse Hanford Company (WHC), 1993]. Based on this study, an interim decision for monitored natural attenuation with institutional controls on groundwater was implemented

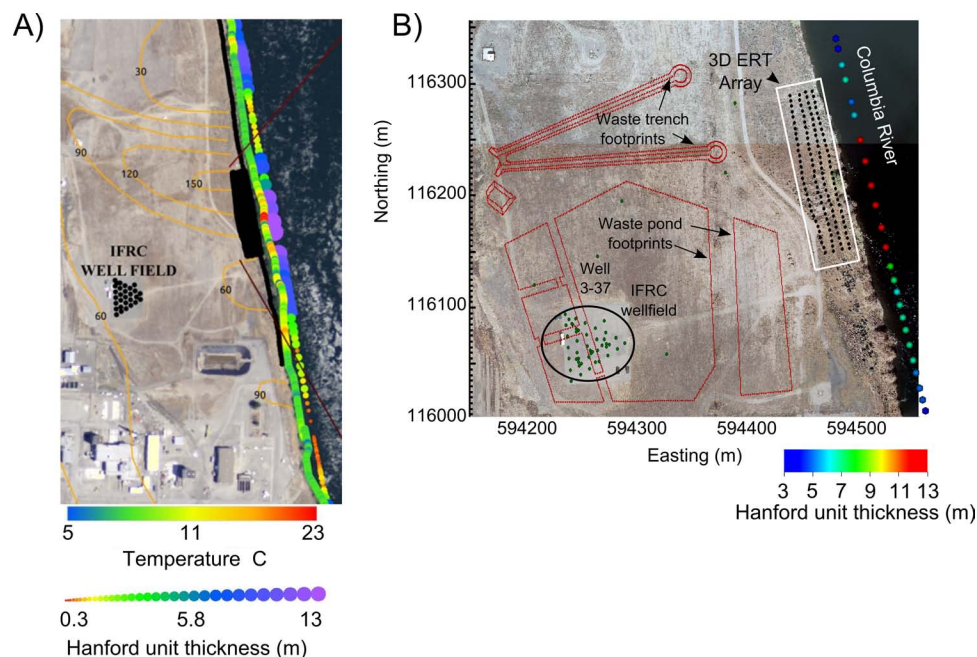


**Figure 1.** Location of the 3-D monitoring ERT array relative to the IFRC wellfield. (a) Temperature anomalies and Hanford unit thickness identified in previous fiber-optic distributed temperature sensing and induced polarization imaging studies [Slater *et al.*, 2010]. (b) Hanford 300 Area, locations of former waste ponds and trenches, IFRC wellfield, Hanford unit thickness [Slater *et al.*, 2010], and surface ERT monitoring array used in this study.

[Environmental Protection Agency (EPA), 1996]. A review in 2006, however, showed that, despite source control measures, groundwater U concentrations remained mostly unchanged [Hartman *et al.*, 2006]. A pressing research need at this site is an improved understanding of the potential for long-term discharge of U from this persistent plume into the Columbia River. To meet this need, the DOE instituted the Hanford 300 Area Integrated Field Research Challenge (IFRC), a multidiscipline, multi-institution research effort to investigate U fate and transport within the 300 Area. The well field installed to assist in this effort is shown in Figure 1 as the IFRC well field. In addition to IFRC studies, achieving a better understanding of U transport also requires studies that capture the spatial distribution of the primary lithologic units along the river corridor as well as spatiotemporal complexity in groundwater-surface water exchange driven by variations in stage levels on the Columbia River. This study was conducted in an effort to obtain multiscale information on the controls of both the underlying hydrogeologic framework and river stage on groundwater-surface water exchange.

[7] The hydrogeologic framework at the Hanford 300 Area is in large part determined by two formations with distinctly different hydraulic properties. The uppermost unit is the Hanford Formation, containing pebble-to-boulder-size gravels and interbedded sands resulting in high hydraulic conductivity (K) of  $\sim 100 \text{ m d}^{-1}$  [Williams *et al.*, 2007]. The underlying unit is the Ringold Formation, a highly heterogeneous unit of granule-to-cobble-size gravels interbedded with fine sand and silt resulting in a lower K of  $\sim 0.2 \text{ m d}^{-1}$  [Williams *et al.*, 2007]. The Hanford-Ringold (H-R) contact is generally considered an important contact that limits vertical migration of contaminants. Identifying the location of the H-R contact is likely critical to determining U transport along the river corridor as the contact topography influences groundwater flow paths and contaminant discharge along the shoreline [Fritz *et al.*, 2007]. The topographic surface of the Ringold was modified by high-energy paleofloods and/or Columbia River flows that eroded into the Ringold Formation [Brown, 1960]. These incised channels, with a northwest-trending erosional axis, were subsequently filled with younger, more permeable Hanford Formation sediments. Although the location and distribution of paleochannels across the 300 Area is currently poorly defined, paleochannels are expected to be  $\sim 10\text{--}20 \text{ m}$  in width [Slater *et al.*, 2010], and they likely govern U transport by providing hydraulically conductive groundwater flow paths through the 300 Area and into the Columbia River during the low river stage. Mapping the locations of these paleochannels is critical to provide an improved understanding of flow and transport along the river corridor in the 300 Area. The current hydrogeological framework for the river corridor at the Hanford 300 Area is largely based on direct probing techniques aimed at determining the elevation of the H-R contact, and projections of the H-R contact onto the riverbed from boreholes drilled inland [Fritz *et al.*, 2007]. This work supports the presence of a hydraulically resistant layer (the Ringold Formation) underlying the uppermost hydrologic unit (Hanford Formation) through which groundwater-surface water exchange and connectivity between the aquifer and the Columbia River is most focused.

[8] Recent research at the 300 Area has confirmed that persistent U concentrations in the groundwater arise as a consequence of both river water chemistry and stage fluctuations [McKinley *et al.*, 2011]. We define the zone of temporally variable water table elevation as the “smear zone.” Unsaturated and smear zone sediments beneath former ponds and trenches have elevated sorbed U concentrations. At high stage, groundwater levels rise into the smear zone, causing desorption and subsequent elevation of U concentrations in the groundwater. In addition, at high stage river water intrudes into the 300 Area. River water is commonly detected at least 250 m inland of the riverbank during spring runoff (Figure 2), and hourly and diurnal changes in stage of over 1 m are known to give rise to some of the fastest groundwater velocities on the Hanford site, with the resulting pressure wave extending as far as 1 km inland [Waichler and Yabusaki, 2005]. The highest desorption rates occur at high stage when river water intrudes into the smear zone beneath former process ponds and trenches. Because of this, improved understanding and modeling of U transport at the 300 Area requires a more detailed characterization of the lithologic heterogeneity that controls river water intrusion into the 300 Area, coupled with direct knowledge of spatiotemporal variability in groundwater-surface water exchange. Our study was designed to demonstrate how time-lapse 3-D resistivity can help address such needs at the required measurement scale.

### 3. Methods

#### 3.1. Three-Dimensional Resistivity Array

[9] Electrical conductivity is a suitable “tracer” for monitoring groundwater-surface water dynamics and the

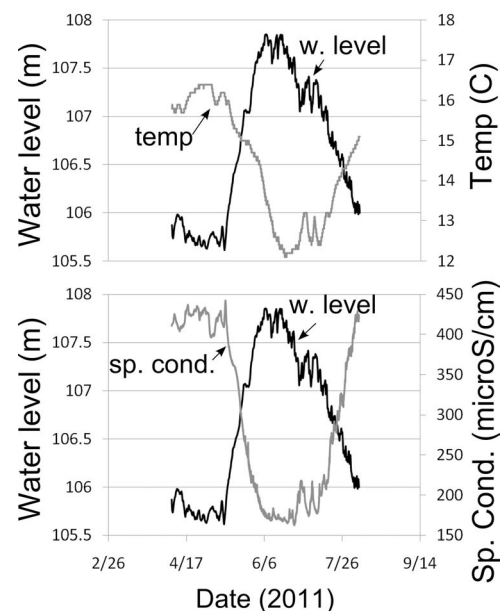


**Figure 2.** Water level elevation with (top) water temperature and with (bottom) specific conductance in well 3-37 (Figure 1) during 2011 spring runoff high stage. The low temperature and conductivity anomalies are caused by river water intrusion.

impact on solute transport at the Hanford 300 Area, because the specific conductance (i.e., the electrical conductivity at 25°C) of groundwater at the site is on the order of 0.040–0.045 S m<sup>-1</sup>, whereas Columbia River water is more dilute (0.015–0.020 S m<sup>-1</sup>) (Figure 2). The contribution of temperature to the bulk conductivity contrast results from the fact that fluid ionic mobility increases with temperature. Groundwater temperature (away from the near shore zone of mixing) is ~15°C–20°C whereas the temperature of Columbia River water varies from 3°C–18°C (there is a contrast of ~5°C except for two summer months; see Figure 2). Both the decreased specific conductance and decreased temperature of river water with respect to groundwater during winter enhance the bulk conductivity contrast between sediments saturated with groundwater and river water. This bulk conductivity contrast enables ERT to detect (in 4-D) when sediments are saturated with river or groundwater, which is the basis for this work.

[10] In October of 2010 we installed a 3-D surface ERT array at the Hanford 300 Area, east of the IFRC well field and close to the river (Figure 1). The array location was chosen based on results from a previous geophysical survey of the riverbed sediments along the river corridor as reported by Slater *et al.* [2010]. This previous study used continuous waterborne electrical imaging (CWEI) to image variations in depth to the Hanford-Ringold contact along a 3-km stretch of the river corridor approximately centered on the IFRC. Slater *et al.* [2010] also performed fiber optic-distributed temperature sensing (FO-DTS) of a 1.6-km stretch of this river corridor to investigate groundwater-surface water exchange at the riverbed. The FO-DTS data set identified persistent temperature anomalies attributed to focused exchange occurring where the Hanford unit was predicted to be thickest from the CWEI survey [Slater *et al.* 2010] (Figure 1a). The 3-D array was centered on a section of the river corridor slightly north of the IFRC well field, where results of the CWEI and FO-DTS identified thick Hanford sediments coincident with temperature anomalies indicative of focused groundwater-surface water exchange (Figure 1b). Note that the FO-DTS data set shown in Figure 1a was acquired on 31 March 2009, when warm temperature anomalies (shown in red) are indicative of groundwater discharge into the river. (See Slater *et al.* [2010], for full details of this study.)

[11] Resistivity data were acquired using an eight-channel resistivity monitoring system. The 3-D array was constructed using 120 electrodes placed at 5 m spacing along each line. Four lines of 30 electrodes each were oriented approximately parallel to the riverbank and spaced ~5 m apart, with minor variations depending on the relief and vegetation (Figure 1b). All electrode locations were georeferenced using a high-precision real-time kinematic (RTK) global positioning system (GPS) system, providing subcentimeter precision when referenced to a benchmark on site. Data were acquired using a combination of dipole–dipole and gradient electrode geometries that used electrodes both along and across the lines. These geometries were selected based on trial measurements that considered signal-to-noise ratio at the site, as well as acquisition rates. A complete set of reciprocal measurements, whereby the voltage and current electrode pairs are exchanged, was obtained for the calculation of individual data errors used in the inversion. The total data set consisted of 17,318 measurements (including

reciprocals) and took ~6 h to collect. The monitoring system typically acquired four complete data sets per day, but occasionally missed collection cycles due to system failure. For time-lapse ERT monitoring, we assume each time-lapse inversion is a “snapshot” of current conditions. Thus, our 6 h survey time requires that we assume river stage is constant over the 6 h survey period. ERT data variability arising from river stage fluctuations that occur at periods of less than 6 h are considered to be noise.

### 3.2. Resistivity Data Filtering

[12] Each data set was filtered in order to remove noisy measurements. Based on an analysis of reciprocal measurements for the first 30 data sets, data were culled if the relative difference between reciprocal measurements exceeded 5% of the observed value, or if the injected current was less than 0.01 A. For time-lapse inversion it was also necessary to reduce each time-lapse data set to a common set of measurements. We used a strict approach for data filtering in this regard, whereby if any measurement fell below the quality criteria in any time-lapse data set, that measurement was culled from every data set. Such strict filtering criteria preserve only the data that are consistently high quality throughout the monitoring period. This filtering strategy yields tomograms with similar spatial resolution and thus facilitates comparison of time-lapse tomograms; however, ease of comparison comes at the expense of possibly eliminating measurement that are high quality in most of the time-lapse data sets. We found that, due to increasing reciprocal errors likely associated with soil drying and subsequent increases in contact resistance, data quality decreased with time so that the number of consistent high-quality measurements was significantly less than the number of data collected during each time-lapse survey. For instance, during the first 20 d of monitoring, 7945 of the 8660 measurements passed the filtering criteria in each data set. After 70 d of monitoring, only 3639 measurements passed the same criteria. We opted to focus our time-lapse analysis on these 3639 measurements taken from each data set in order to allow continuous analysis of the entire 70 day monitoring period. Sensitivity plots were investigated to ensure that the reduced set of measurements maintained adequate resolution within the model space. We used 273 data sets collected from 17 November 2010 to 22 February 2011 to produce the bulk conductivity time series we compared to river stage as shown in section 4.2.

### 3.3. Time-Lapse Inversion Processing

[13] Data were weighted according to the criteria proposed by LaBrecque and Yang [2001], which gives the standard deviation of each measurement as,

$$\sigma_i = \alpha d_{obs,i} + \beta, \quad (1)$$

where  $\sigma_i$  is the standard deviation of measurement  $i$ ,  $d_{obs,i}$  is the observed transfer resistance for measurement  $i$ ,  $\alpha$  is a scalar weighting parameter which scales the standard deviation according to the magnitude of  $d_{obs,i}$ , and  $\beta$  is a measure of instrument precision and prevents small transfer resistance measurements from having excessively small standard deviations and dominating the inversion. Based on analysis of the reciprocal measurements, we determined

$\alpha = 0.05$  and  $\beta = 0.001$  ohms. We used the normalized  $\chi^2$  statistic as the convergence criteria which is given by,

$$\chi^2 = \frac{1}{N_d - 1} \sum_{i=1}^{N_d} \left( \frac{d_{\text{pred},i} - d_{\text{obs},i}}{\sigma_i} \right)^2. \quad (2)$$

[14] Here  $d_{\text{pred},i}$  is the simulated transfer resistance for measurement  $i$ . If the data are appropriately weighted given the actual (but unknown) noise, and data noise is normally distributed, then  $\chi^2 = 1$ .

[15] To construct the time-lapse sequence we inverted the first data set collected on 17 November 2010 to produce a baseline conductivity distribution. We regularized this inversion with isotropic first-order spatial derivative smoothing constraints. The results of this inversion serve as both the starting and reference model for the subsequent time-lapse inversions. To construct each time-lapse inversion, equation (2) is computed using the predicted data from the starting model and the observed data from the current time-lapse data set. If the  $\chi^2$  criterion is not satisfied at the starting model, the inversion procedure updates the starting model using a parallel Gauss-Newton iteration procedure. Each time-lapse inversion is regularized by the smoothing operator described in Appendix A. The temporal constraints are provided by minimizing the difference between the baseline and time-lapse solutions, subject to fitting the data. Thus, deviations from the baseline bulk conductivity occur in each time-lapse solution only if required by the data in order to meet the convergence criteria. It is important to note that the imaging results provided by ERT are of limited and spatially variable resolution, meaning that each time-lapse image is a smoothed representation of the actual subsurface bulk-conductivity distribution. This smoothing will cause the results of the time series and time-frequency analysis to also be smoothed in space.

[16] We inverted the data using the parallel ERT modeling and inversion code described by *Johnson et al.* [2010]. We used an unstructured tetrahedral mesh with refinement near electrodes and within the “imaging zone.” The mesh surface topography was constructed using LIDAR data collected at the site that has a horizontal resolution of  $\sim 40$  cm and a vertical resolution of  $\sim 30$  cm. The mesh consists of 37,630 nodes and 198,750 elements, and each inversion was executed on 121 processors. The baseline inversion required  $\sim 30$  min of compute time and each time-lapse inversion required between 2 and 10 min depending on how far each time-lapse solution deviated from the starting model. We next discuss two approaches, time series analysis and time-frequency analysis, to extracting the key hydrological information from the inversion results.

### 3.4. Time Series Analysis: Correlation, Lag Time, and Coefficient of Variation

[17] The decrease in both the specific conductance and temperature of river water compared to groundwater during the survey period enables ERT to image zones of stage-driven groundwater-surface water exchange. As the stage increases, lower salinity river water flows into the formation and replaces groundwater in the saturated pore spaces beneath the array, causing a decrease in bulk conductivity.

When the stage decreases and the mixing front retreats toward the river, pore spaces are filled with higher-salinity groundwater, and bulk conductivity increases. As noted earlier, the temperature difference between groundwater and surface water during the winter months accentuates the conductivity contrast due to salinity alone. The rich hydrological information on this extensive time-lapse data set (273 surveys in total) cannot be conveniently presented by plotting images of resistivity change over time. In this section we therefore describe three methods of analyzing the bulk conductivity time series in each inversion element along with the river-stage time series to identify the dominant regions of exchange. These three methods are valid as long as the groundwater-surface water mixing front is within the ERT imaging zone (i.e., beneath the array) during the monitoring period.

[18] 1. Correlation: For the reasons described in the previous paragraph, we expect a negative correlation between river stage variations and bulk conductivity variations in the saturated zone when exchange is occurring within the support volume of the array. We expect this negative correlation to be enhanced in the more permeable areas of the aquifer that are highly connected to the river because river water is more free to advance and retreat within the aquifer in these zones. The cross-correlation coefficient between bulk conductivity within a particular inversion element and stage at time lag  $t$  is given by,

$$\text{corr}(t) = \frac{1}{N_k} \sum_{k=0}^{N_t-t} \left( \frac{C_{t+k} - \bar{C}}{\sigma_c} \right) \left( \frac{S_k - \bar{S}}{\sigma_s} \right), \quad (3)$$

where  $N_t$  is the number of stage and conductivity values in the time sequence,  $N_k = N_t - t$ ,  $C_k$  is the bulk conductivity at time  $k$ ,  $\bar{C}$  is the mean conductivity of the time sequence,  $\sigma_c$  is the standard deviation of the conductivity time sequence,  $S_k$ ,  $\bar{S}$ , and  $\sigma_s$  are the corresponding stage time series, mean, and standard deviation.

[19] 2. Lag time to maximum correlation: The time lag,  $t_{\text{max}}$ , to maximum absolute correlation in a particular inversion element indicates the time required for river water to reach that element after an increase in stage. Elements further from the river should exhibit a longer lag time to maximum correlation than elements next to the river. Furthermore, elements in more permeable zones connected to the river should exhibit relatively shorter lag times because pore water will travel more quickly in these zones given the same stage-induced gradient. We therefore expect lag time to maximum correlation to be indicative of preferred flow channels.

[20] 3. Bulk conductivity coefficient of variation: The coefficient of variation is a measure of the variability in the bulk conductivity time series [*Nenna et al.*, 2011], and is given by,

$$C_{\text{var}} = \frac{\sigma_c}{\bar{C}}. \quad (4)$$

[21] We would expect inversion elements in more permeable zones to exhibit higher variation coefficients because river water replaces groundwater and alters bulk conductivity more readily in these zones than in less-permeable zones. As we will demonstrate, the coefficient of variation

is also a useful companion statistic to correlation because it gives an indication of the relative magnitude of stage-driven changes in conductivity that are not evident by the correlation statistic alone.

[22] Correlation, lag time, and coefficient of variation are valid as long as the relationship between river stage and bulk conductivity within the image zone is constant in time. As we will show, this assumption is well founded for the application demonstrated here. If the relationship between stage and bulk conductivity is time dependent, correlation, lag time, and coefficient of variation will give misleading results. This may occur, for instance, during a high river stage when the mixing front has moved far inland of the monitoring array. Short period stage variations around the time of the high stage will cause the location of the mixing front to oscillate, but the pore space below the monitoring array will be occupied by river water regardless, and there will be no change in bulk conductivity arising from stage variations. During such a high stage period there will be no correlation between stage and bulk conductivity, and the resulting correlation analysis will be uninformative because the correlation operator considers the entire time series at once. Such time dependency in the river stage/bulk conductivity relationship can be accounted for using time frequency analysis as described in section 3.5. In addition, although we expect no correlation between the stage and bulk conductivity in the unsaturated zone, a positive correlation is observed. We use a synthetic example in section 4 to demonstrate that this correlation is an artifact arising from the combined effects of the variable water table, the nonlinearity of the inverse problem (and subsequent conductivity-dependent sensitivity), and the regularization constraints.

### 3.5. Time-Frequency Analysis

[23] The fast Fourier transform (FFT) has been applied widely to process different geophysical data [Denker and Wenzel, 1987; Forsberg, 1985]. However, the FFT method is unsuitable for analyzing a nonstationary geophysical time series since the method only provides time-averaged amplitude and it does not provide information about the changes of frequency content with time [Stockwell et al., 1996; Tsoulis, 2003]. Stage variations driven by complex dam operations result in strong nonstationarity in the stage time series. Nonstationarity in the voxel bulk conductivity time series can also be anticipated if the mixing zone advances and retreats through the electrical imaging zone as noted in section 3.4. To address the FFT limitations, methods such as the Continuous Wavelet Transform (CWT) have been applied extensively to analyze nonstationary signals [Gamage and Blumen, 1993; Kumar, 1997; Torrence and Compo, 1998; Haus and Graber, 2000; Grinsted et al., 2004; Henderson et al., 2009]. Of particular relevance to our work are recent papers by Pidlisecky et al. [2011], who studied soil-moisture dynamics using wavelet analysis of electrical data, and Linde et al. [2011], who used wavelet analysis to correlate hydrologic and self-potential signals. Unlike the FFT and CWT, the Stockwell (S) transform uniquely combines a frequency-dependent resolution of the time-frequency space with absolutely referenced local phase information [Stockwell, 1999]. Stockwell [1999] derived the S-transform from the short-time Fourier

transform (STFT) as follows. The time average spectrum  $H(f)$  for a given time series  $h(t)$  is given by,

$$H(f) = \int_{-\infty}^{\infty} h(t)g(t)e^{-i2\pi ft} dt, \quad (5)$$

where  $f$  is the frequency of different periods within the signal,  $t$  is time, and  $g(t)$  is a Gaussian function used to window the time series  $h(t)$ .

[24] The S-transform uses a Gaussian function with a width depending on the local frequency under investigation, the dilation ( $\tau$ ), and translation of the wavelet. The Gaussian function  $g(t)$  is given by,

$$g(t) = \frac{f}{\sqrt{2\pi}} e^{-\frac{(\tau-t)^2 f^2}{2}}. \quad (6)$$

[25] Combining equations (5) and (6), the S-transform is defined as,

$$S(\tau, f) = \int_{-\infty}^{\infty} h(t) \frac{f}{\sqrt{2\pi}} e^{-\frac{(\tau-t)^2 f^2}{2}} e^{-i2\pi ft} dt. \quad (7)$$

[26] As shown in equation (7),  $S(\tau, f_1)$  is a one-dimensional vector, which contains the changes of amplitude and phase over  $h(t)$  for a particular frequency  $f$ . This equation is applied to all frequencies within the signal. The net result of the S-transform is a complex matrix whereby the rows of that matrix are different frequencies at particular time values (columns).

[27] We also performed a two-dimensional (2-D) S-transform analysis by simultaneously running the 1-D S-transform analysis at a specific frequency on all individual elements within the ERT image sequence. The net result of this step is a complex vector whereby the values illustrate how the amplitude for a specific frequency within the frequency spectrum changes with time at each location. The 1-D S-transform was then run for a single instance in time but across space within the image to see how the amplitude at a specific frequency changes with space. The 2-D S-transform image was then produced by averaging the observed results at each location over a certain period (performed here every 2 weeks) [Mansinha et al., 1997], and performing this calculation at all locations. The resulting 2-D S-transform image depicts the conductivity variations at a specific frequency of interest within the ERT model space.

## 4. Results

### 4.1. Baseline Inversion Results

[28] Figures 3a and 3b show plan and oblique views, respectively, of the baseline inversion result. The imaged volume is sliced parallel to the electrode lines and shown with a transparent color scale and an iso-surface at  $0.02 \text{ S m}^{-1}$  to highlight a depression in the bulk conductivity iso-surface. The fine-grained Ringold Formation sediments exhibit increased electrical conductivity with respect to the coarser-grained Hanford Formation sediments such that bulk conductivity can be used to map the relative topography of the H-R contact. The depression in the bulk conductivity iso-surface revealed by the baseline inversion indicates



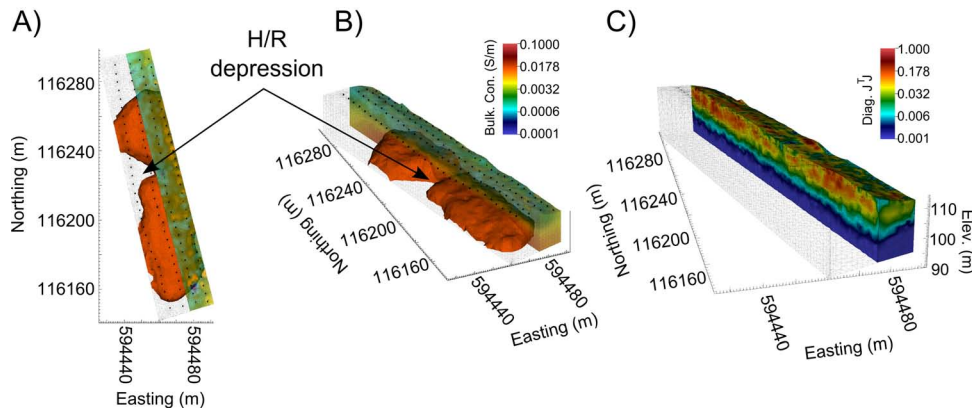


**Figure 3.** (a) Plan and (b) oblique view of 3-D ERT baseline inversion results. The 3-D block is sliced to reveal the location of a targeted Hanford/Ringold contact depression (a presumed paleochannel). The bulk conductivity iso-surface is at  $0.02 \text{ S m}^{-1}$ . (c) Diagonal elements of  $J^T J$  where  $J$  is the weighted sensitivity matrix.

a corresponding depression in the H-R contact, and provides a candidate location for an incised high-permeability paleo-channel providing a preferred flow pathway for stage-driven groundwater-surface water exchange.

[29] The sensitivity map in Figure 3c shows the diagonal elements of  $J^T J$ , where  $J$  is the weighted sensitivity matrix. The diagonal elements of  $J^T J$  contain the sum of the squared sensitivities of the data to each element. The sensitivities show a relatively uniform distribution at a given depth, indicating that the H-R contact depressions in Figures 3a and 3b are not artifacts associated with variable image sensitivity due to the measurement configuration. Furthermore, this depression corresponds with a thickening of Hanford sediments in the same location in the river bed identified by Slater *et al.* [2010] (see their Figure 2a), which was used to guide placement of the 3-D monitoring array. A key objective of the ERT monitoring campaign was then to determine if this H-R depression provides a “gateway” for preferential groundwater-surface water exchange into the 300 Area.

#### 4.2. Time Series Analysis

[30] Figure 4 shows the river stage over the monitoring period along with the bulk conductivity for several elements that are highly correlated to stage. This figure illustrates the nonstationarity of both the river stage and element conductivities. Figures 4b and 4d show the bulk conductivity time series of example elements below the water table, while Figures 4c and 4e show example elements above the water table. The time series shown in Figures 4d and 4e are scaled by subtracting the mean from each time series and dividing the results by the standard deviation as shown by the correlation computation in equation (3). The example element locations corresponding to Figures 4b–4e are shown in Figure 4f.

[31] The bulk conductivity time series shown in Figures 4b and 4d exhibit the behavior we expect given hydraulic communication with the river. Bulk conductivity fluctuations show strong negative correlation to the river stage as predicted. In addition, we observe a lag time in the bulk conductivity decrease in response to a corresponding increase in

stage and vice-versa (note the peaks in conductivity lagging behind the troughs in stage in Figure 4d). As discussed previously, this lag time is related to the time required for river water to infiltrate or evacuate the aquifer at the element location after an increase or decrease in the stage.

[32] Figure 5a shows the maximum correlation between stage and bulk conductivity throughout the imaging volume as computed by equation (3). We readily observed that the bulk conductivity is negatively correlated to the stage below the water table and positively correlated to the stage above the water table. Figure 5b shows the lag time to maximum correlation throughout the imaging volume. In general, lag times are zero or very small throughout the unsaturated zone and larger below the water table. Long lag times exhibited in the elements above the water table are meaningless because they are always associated with low correlation values (see Figure 5a). Figure 5c shows the coefficient of variation in bulk conductivity throughout the imaged zone, and demonstrates that relative changes in bulk conductivity are small in the unsaturated zone compared to the saturated zone. Figure 5 clearly shows that, although the estimated bulk conductivity variations above the water table are highly correlated to the stage (Figure 5a), the magnitudes of those variations are quite small (Figure 5b). The fact that lag times to maximum correlation (Figure 5b) are small above the water table indicates that the estimated bulk conductivity variations above the water table are associated with water table elevation, which responds practically instantaneously with the stage. We demonstrate that these bulk conductivity variations arise as a consequence of stage-driven sensitivity variations in the unsaturated zone with a forthcoming synthetic example. We first turn our attention to the correlations, lag times, and bulk conductivity variations beneath the water table.

#### 4.3. Correlation, Lag Time, and Coefficient of Variation in the Saturated Zone

[33] Figure 6 shows the maximum correlation, time lag, and coefficient of variation at selected elevations beneath the water table. Baseline bulk conductivity contours are superimposed on the images at each elevation in order to

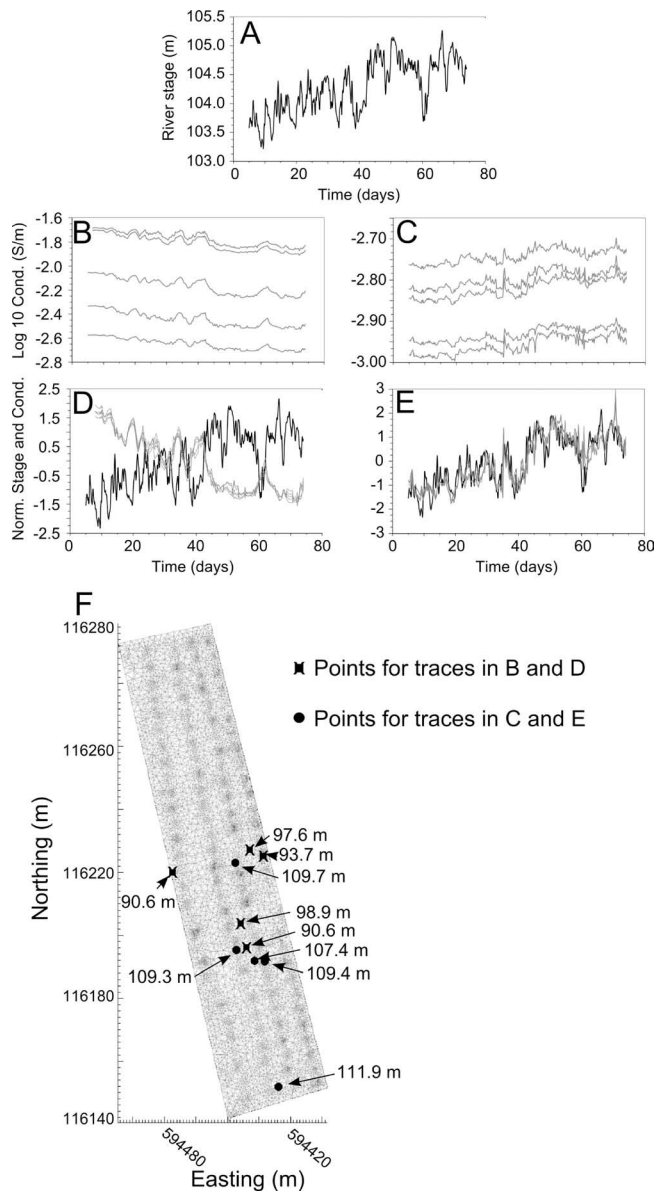


**Figure 4.** (a) River stage above sea level with time. (b) Example bulk conductivity time series from elements below the water table with maximum correlation to river stage below  $-0.85$ . (c) Example bulk conductivity time series from elements above the water table with maximum correlation values above  $0.85$ . (d) Comparison of scaled stage (black lines) and bulk conductivity (gray lines) for the time series shown in Figure 4b. (e) Comparison of scaled stage (black lines) and bulk conductivity (gray lines) for the time series shown in Figure 4c. (f) The locations of the five elements below and above the water table with elevations labeled.

show the location of the bulk conductivity iso-surface depression marking the paleochannel. As shown in Figure 6a, bulk conductivity displays a strong negative correlation to stage throughout the saturated zone, ranging from  $-0.7$  to  $-0.9$ . This is expected since, for example, river water will eventually replace groundwater throughout the imaging zone during a sustained high stage. Furthermore, we observe the most

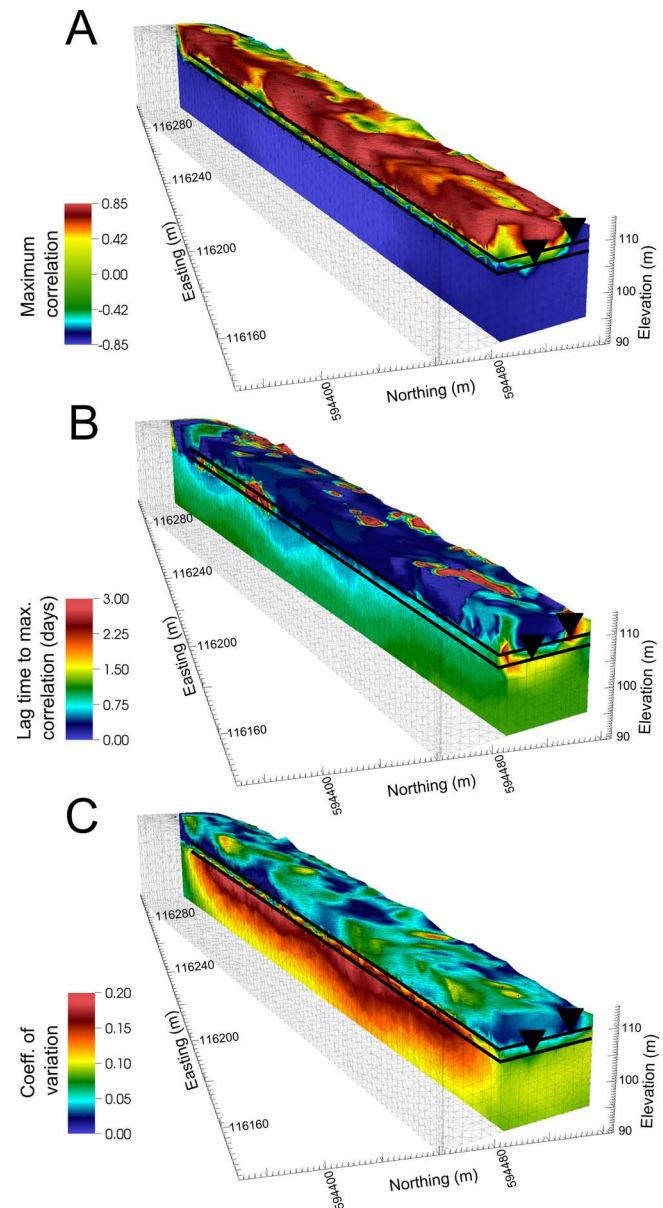


**Figure 5.** (a) Maximum correlation coefficient between stage and bulk conductivity within the imaged volume. (b) Lag time to maximum correlation. (c) Coefficient of variation of the bulk conductivity time series.

negative correlations to occur directly over the target bulk conductivity iso-surface depression assumed to represent a zone of extensive exchange. In addition, correlation generally tends to decrease where baseline bulk conductivity increases. This is expected as exchange is likely to be suppressed in the finer-grained materials represented by the higher bulk conductivity values.

[34] Lag time to maximum correlation is arguably the most useful statistic in Figure 6 because it is directly related to pore water velocity, and therefore to permeability. We observe that lag times are shortest within the bulk conductivity depression at each depth, and shortest overall near the water table where sediments are likely to be coarsest (i.e., well above the Ringold Formation), suggesting



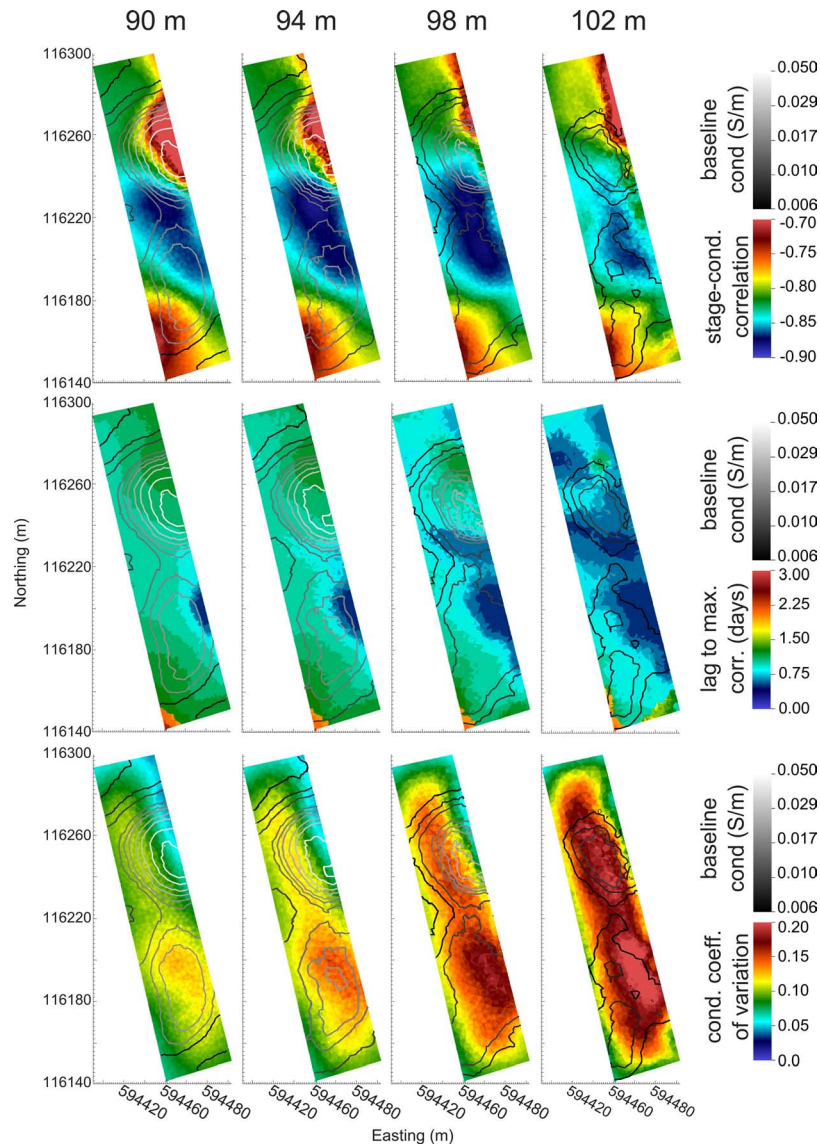


**Figure 6.** (Top row) Correlation coefficient, (middle row) lag time, and (bottom row) coefficient of variation at selected depths below the water table. The gray scale contours show the baseline bulk conductivity superimposed on each plot at depth. Maximum correlations and minimum lag times occur within the presumed paleochannel marked by the baseline bulk conductivity depression.

that pore water velocities are greatest in these zones. Lag times increase with distance from the river (both horizontal and vertical), and are generally longer in regions of increased baseline conductivity (i.e., finer-grained materials), suggesting lower pore water velocities in these zones. Note that both the correlation and lag time plots suggest a northwest-trending high permeability feature overlying the H-R contact low in the baseline conductivity image. Northwest-trending paleochannels are expected in the 300 Area given the depositional history [Brown, 1960].

[35] The coefficient of variation plot shows the regions of greatest stage-driven variability in bulk conductivity. We observe that the greatest variability occurs near the water table where sediments are likely to be coarsest (i.e., well above the Ringold Formation). Variability decreases with depth as sediments become finer and the distance to the river increases. The regions of greatest variability

correlate to the regions of the smallest lag times (i.e., regions of highest pore velocity) and the regions of greatest (negative) stage-conductivity correlation. Each plot indicates active exchange above the H-R low stage shown in the baseline conductivity image (Figure 3).

#### 4.4. Bulk Conductivity Variations Above the Water Table

[36] Figures 4c and 4e show pervasive bulk conductivity responses above the water table that can be explained with the help of Figures 5 and 7. Figures 4 and 5 show that elements above the water table in general display a strong, zero-phase, positive correlation with stage. In other words, an increase in stage is “immediately” followed by an increase in the estimated bulk conductivity above the water table. This response in estimated bulk conductivity above the water table is not physical. Instead, it is an inversion

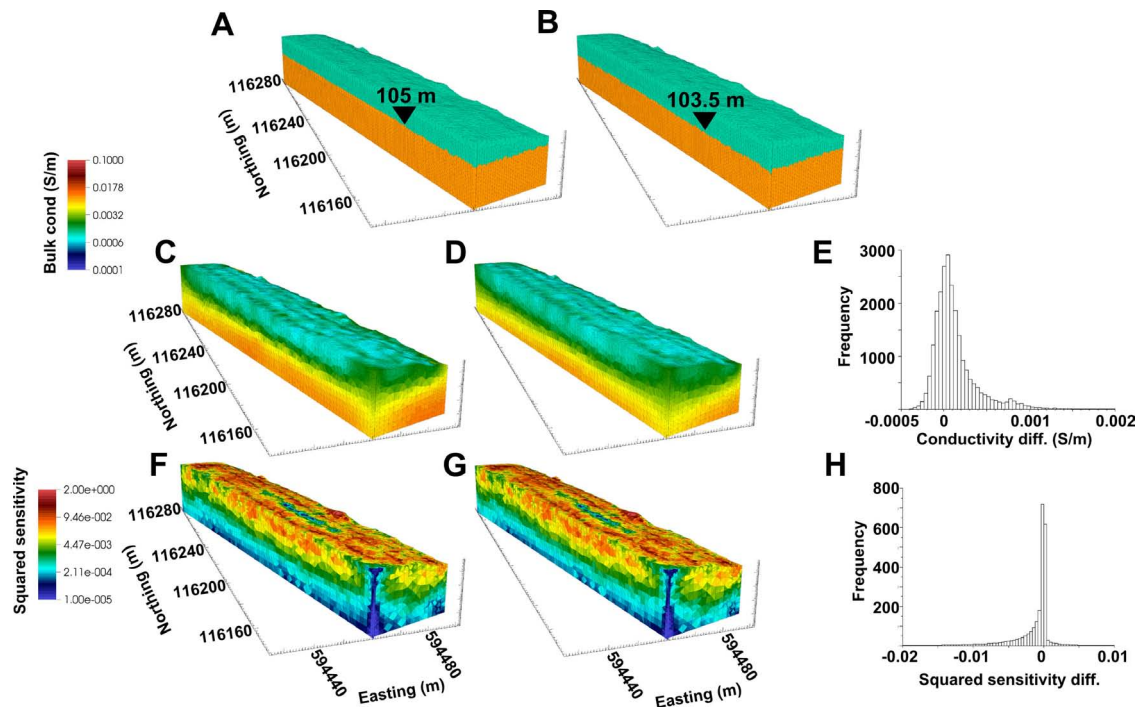


**Figure 7.** (a) Synthetic bulk conductivity distribution representing the water table at 105 m and (b) 103.5 m, which are approximately the maximum and minimum water table elevation over the survey period (see Figure 4B). (c) ERT estimated bulk conductivity distribution for 105 m and (d) 103.5 m water table. (e) Histogram of conductivity differences between 105 m and 103.5 m inverse solutions for all elements in the vadose zone above 105 m. (f) Sensitivity distribution for 105 m and (g) 103.5 m inversion. (h) Histogram of difference in sensitivity between 105 m and 103.5 m inversions for all elements above 105 m.

artifact originating in the nonlinearity of the inverse problem (i.e., the dependence of the bulk conductivity sensitivity on the bulk conductivity itself). We demonstrate this with inversions performed on two synthetic models designed to simulate the time-lapse survey.

[37] Figures 7a and 7b show synthetic conductivity distributions approximating water table elevations at 105 and 103.5 m, respectively. These are the approximate maximum and minimum river stage elevations during the monitoring period (Figure 4). Note that, because of the high permeability of the Hanford Formation, the water table elevation closely tracks the river stage, such that both stage and water table elevation can be considered equivalent at a given point in time for the purposes of this study. We simulated ERT surveys on a fine mesh to produce synthetic data corresponding to each water table elevation, added 5% random noise, and inverted each to produce the estimated conductivity distributions shown in Figures 7c and 7d. Figure 7e shows a histogram of the conductivity estimated at the 105 m water table elevation minus that estimated at the 103.5 m elevation, for all elements above 105 m (i.e., the unsaturated zone elements). The histogram shows that estimated unsaturated zone conductivities are slightly larger when the water table is higher, just as it is observed in the real ERT monitoring results. Figures 7f and 7g show the sensitivity distributions corresponding to the solutions in Figures 7c and 7d, respectively. Figure 7h shows the histogram of the 105 m inversion sensitivities minus those of the 103.5 m inversion

for the elements above 105 m. This histogram shows a decrease in unsaturated zone sensitivity at the higher water table. This sensitivity decrease encourages the slight increase in the estimated unsaturated zone conductivity. In addition, regularization smoothing into the unsaturated area from the smear zone during the high stage may also contribute to the elevated unsaturated zone conductivity. These two effects ultimately explain the apparent nonphysical positive correlation between stage and conductivity above the water table.

#### 4.5. Time-Frequency Analysis

[38] Figure 8 shows the results of the 1-D S-transform analysis for the river stage (Figure 8a), bulk conductivity time series for two example elements located inside the paleochannel at varying depths below the water table shown in Figure 4b (Figure 8b), the bulk conductivity time series for two elements located outside the paleochannel at similar depths as those shown in Figure 4b (Figure 8c). The river-stage time series (Figure 8a) shows significant short period variations with time. As discussed previously, those variations will cause the mixing front to move continuously with time.

[39] The S-transform analyses for example elements located inside and outside the paleochannel at elevations 94 and 99 m exhibit the same 8-, 16-, and 32-d periods observed in the stage data set, providing further evidence that the stage variations drive the conductivity variations in the saturated zone. Furthermore, the strength of different

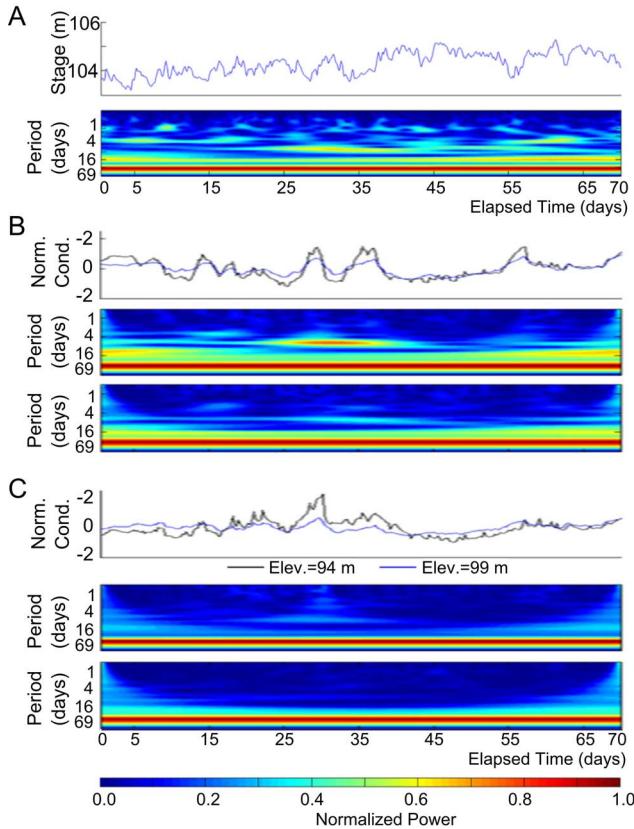


**Figure 8.** Example time-frequency analysis of the 3-D ERT survey showing S-transform results of (a) river stage, (b) voxels located inside the paleochannel at varying depths below the water table, and (c) voxels located outside the paleochannel at similar depths as in Figure 8b.

periods obtained from the S-transform analysis for these elements is probably related to the distribution of preferential flow paths. For example, the S-transform section for the elements located inside the paleochannel contains stronger 8- and 16-d periods than elements outside of the paleochannel, indicating that these elements are probably in a region with higher connectivity between surface water and groundwater. A key feature of the S-transform is its ability to narrow down the times within the time series that the groundwater-surface-water-mixing front is within a particular element. This is clearly demonstrated in Figures 8a and 8b, which shows strong 8-d period oscillations focused around days 25–35 in both stage and conductivity, indicating that during this period groundwater and river water are exchanging with these elements. In addition, the magnitude of the 16-d period changes around the same days in both stage and conductivity.

[40] To extend this analysis further, we show the 2-D S-transform analysis at the 8- and 16-d periods to highlight both the spatial and temporal variations in the strength of these periods (that are strong in the stage data) across the entire model space. Figure 9c shows the results of this analysis. The boxed region indicates the depression in the H-R contact. The 8-d period analysis illustrates that the highest normalized power is concentrated within the region of the depression of the H-R contact. Furthermore, the ability of

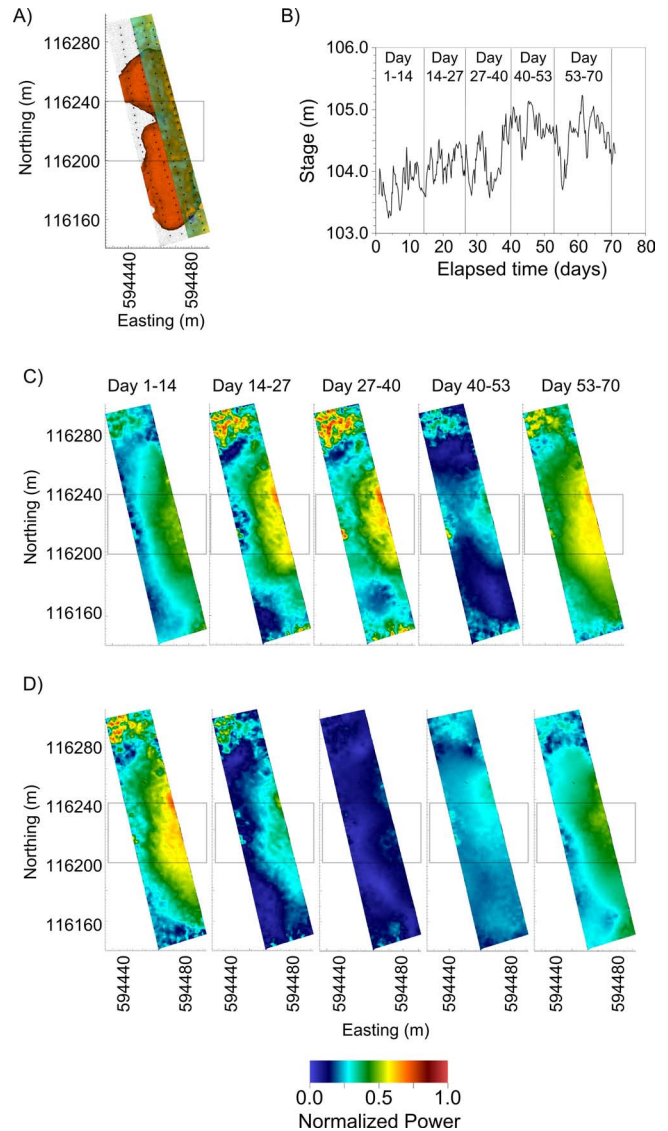


**Figure 9.** (a) ERT inversion results with H-R low highlighted. (b) River stage elevation over monitoring period, including time-frequency analysis divisions for comparison to Figures 9c and 9d. (c) Normalized power from the S-transform at an elevation of 99 m and a period of 8 d. (d) Normalized power from the S-transform at an elevation of 99 m and a period of 16 d. The boxed region shows the H/R low (see Figure 9a.)

the S-transform to isolate times when the exchange is focused below the array versus the suppressed times due to the exchange occurring outside of the array is clear in these images. For example, exchange beneath the array was clearly weaker during days 40–53.

## 5. Discussion and Conclusions

[41] Continuous, high-temporal resolution resistivity imaging is an emerging technology that can be autonomously deployed to noninvasively investigate hydrological processes. The temporally rich data that can now be obtained with this method, as we have demonstrated here, mandate new approaches to processing and interpreting such data sets in a



manner that concisely captures the hydrological information available in such data sets. We have presented a new approach to analyzing large time-lapse 3-D resistivity data sets based on time series analysis and time-frequency analysis and demonstrated the approach for improving understanding of the dynamics of groundwater-surface water exchange along a major river corridor.

[42] We have demonstrated the use of both relatively simple descriptors of the element conductivity time series (correlation, lag time and coefficient of variation), and time-frequency analysis (based on the S-transform), to capture spatial and temporal changes in groundwater-surface water exchange. The time series descriptors clearly identify the relative activity of stage-driven exchange and provide information concerning 3-D pore velocities. These descriptors are relatively easily computed and capture spatial variability in the time-averaged behavior of the system. However, they do not readily provide information on the time dependency of these descriptors, and may provide misleading results if the stage/bulk-conductivity relationship changes with time. Time-frequency analysis, although more computationally demanding, has the advantage of revealing time dependency in the system behavior. These advantages were demonstrated in our study as the 2-D S-transform captures temporal variability in the strength of exchange occurring beneath the electrode array (Figure 8). Furthermore, the frequency analysis permits identification of the driving periodicities in the river stage that exert the dominant control on groundwater-surface water exchange, thereby leading to a more complete interpretation of the system dynamics.

[43] We have demonstrated the utility of time series and time-frequency approaches for analyzing temporally rich resistivity data sets using a study of a major river corridor where complex stage oscillations are known to exert a strong control on U desorption and transport of U-contaminated groundwater. Our resistivity imaging survey noninvasively captured spatiotemporal variability in groundwater-surface water exchange associated with hydrogeological heterogeneity and variable stage-driven forcing. Our analysis illuminated a zone of preferred groundwater-surface water exchange associated with a depression in a high-conductivity underlying unit that represents a semiconfining clay formation. Our results strongly suggest that this depression is a conduit for preferential exchange and likely plays an important role in determining the connectivity between river water and U-contaminated groundwater at this site.

[44] Our study has also highlighted potential limitations of the applied approaches if physically meaningless resistivity variations exist in the time lapse images. Artifacts in resistivity images resulting from the mechanics and limitations of inverse routines can often impede efforts to extract hydrogeological information from time-lapse resistivity data sets [Day-Lewis *et al.*, 2005]. We have shown that similarly, caution must be used to prevent misinterpretation of unphysical signals that result from inversion artifacts being mapped into the time series analysis. For example, we used synthetic simulations to show that high correlations between river stage and bulk conductivity recorded in the unsaturated zone can be explained by an inversion artifact associated with variable image sensitivity driven by minor changes in the water level. In this case, the coefficient of

variation computed from the time series indicated that these high-correlation zones were unlikely to be hydrologically important.

[45] Approximately 6 yr ago, fiber optic-distributed temperature sensing was introduced as a technique to advance understanding of groundwater-surface water exchange on stream beds via the collection of temperature data sets with unique high spatiotemporal resolution. We argue that high-resolution 3-D resistivity imaging as applied in this study has a similar potential to further advance the understanding of groundwater-surface water interactions by providing unique information on the dynamics of exchange beyond the streambed. The time series and time-frequency analysis techniques described here represent approaches to optimize the hydrological interpretation retrievable from such temporally rich resistivity 3-D data sets. Such approaches also have the potential to improve the understanding of other dynamic hydrological processes that have associated electrical resistivity contrasts.

## Appendix A

[46] Let the vector  $\mathbf{m}_t$  represent the bulk conductivity distribution (or inverse solution) at time  $t$ . The regularization constraints specify that

$$\nabla \left( \frac{\partial}{\partial t} m_t \right) = 0. \quad (\text{A1})$$

[47] In words, temporal changes in the inverse solution should have a small spatial derivative. Equation (A1) is satisfied exactly if the inverse solution does not change over time and is implemented as follows. Let  $m_{1,t}$  and  $m_{2,t}$  represent the bulk conductivity in adjacent mesh elements (1 and 2) at time  $t$ , and let  $m_{1,\text{ref}}$  and  $m_{2,\text{ref}}$  represent the same elements at some reference time. Equation (A1) is approximately satisfied if,

$$\partial m_2 - \partial m_1 = m_{1,t} - m_{2,t} + m_{2,\text{ref}} - m_{1,\text{ref}}, \quad (\text{A2})$$

where  $\partial m_1$  and  $\partial m_2$  represent the bulk conductivity updates to  $m_{1,t}$  and  $m_{2,t}$  as determined by the inversion procedure. Equation (A2) represents one regularization constraint equation. One such equation is specified in the time-lapse inversion for each adjacent element pair in the mesh.

[48] **Acknowledgments.** We appreciate helpful reviews provided by Larry Bentley, Adam Pidlisecky, and an anonymous reviewer. This work was funded by the Department of Energy Subsurface Biogeochemical Research Program, through grant DE-AI02-08ER64565. Additional support was provided by the U. S. Geological Survey Toxic Substances Hydrology Program. Time-lapse ERT inversion capabilities leveraged in this research were developed under support from the Office of Biological and Environmental Research, U. S. Department of Energy, as part of the Hanford 300 Area Integrated Field Research Challenge project, and the Office of Environmental Management, U. S. Department of Energy, as part of the Deep Vadose Zone Applied Field Research Initiative. Inverse computations for this research were performed using the Pacific Northwest National Laboratory Institutional Computing system. The authors gratefully acknowledge field assistance from Kisa Mwakanyamale and Jason Greenwood.

## References

- Acworth, R., and G. Dasey (2003), Mapping of the hyporheic zone around a tidal creek using a combination of borehole logging, borehole electrical tomography, and cross-creek electrical imaging, New South Wales, Australia. *Hydrogeol. J.*, 11(3), 368–377.

- Binley, A., B. Henry-Poulter, and B. Shaw (1996), Examination of solute transport in an undisturbed soil column using electrical resistance tomography, *Water Resour. Res.*, 32(4), 763–769.
- Brown, D. J. (1960), *Evaluation of Earth Samples From Churn-Drilled Wells*, 26 pp., Hanford Atomic Products Operation, Richland, Wash.
- Crook, N., A. Binley, R. Knight, D. Robinson, J. Zarnetske, and R. Haggerty (2008), Electrical resistivity imaging of the architecture of substream sediments, *Water Resour. Res.*, 44, W00D13, doi:10.1029/2008WR006968.
- Day-Lewis, F., K. Singha, and A. Binley (2005), Applying petrophysical models to radar travel time and electrical resistivity tomograms: Resolution-dependent limitations, *J. Geophys. Res.*, 110(17), B08206, doi:10.1029/2004JB003569.
- Denker, H., and H. Wenzel (1987), Local geoid determination and comparison with GPS results, *Bull. Geod.*, 61, 349–366.
- de Voogd, N., and H. den Rooijen (1983), Thin-layer response and spectral bandwidth, *Geophysics*, 48, 12–18.
- Environmental Protection Agency (EPA) (1996), *Declaration of the Record of Decision for the 300-FF-1 and 300-FF-5 Operable Units*, 49 pp., Washington, D.C.
- Forsberg, R. (1985), Gravity field terrain effect computations by FFT, *Bull. Geod.*, 59, 342–360.
- Fritz, B., N. Kohn, T. Gilmore, D. McFarland, E. Arntzen, R. Mackley, and A. Bunn (2007), Investigation of the hyporheic zone at the 300 Area, Hanford site, *Rep. PNNL-I6805*, Pacific Northwest National Laboratory, Richland, Wash.
- Gamage, N., and W. Blumen (1993), Comparative analysis of low-level cold fronts: Wavelet, Fourier, and empirical orthogonal function decomposition, *Mon. Weather Rev.*, 121, 2867–2878.
- Grinsted, A., J. Moore, and S. Jevrejeva (2004), Application of the cross wavelet transform and wavelet coherence to geophysical time series, *Nonlinear Proc. Geoph.*, 11, 561–566.
- Hartman, M., L. Morasch, and W. Webber (2006), Hanford site groundwater monitoring for fiscal year 2005, *Rep. PNNL-I5070*, 61 pp., Pacific Northwest National Laboratory, Richland, Wash.
- Haus, B. K., and H. C. Graber (2000), Analysis of non-stationary vector fields using wavelet transforms, *Proc. Oceans 2000 MTS/IEEE Conf.*, Vol. 3, pp. 1521–1527, MTS/IEEE, Providence, RI.
- Henderson, R., F. Day-Lewis, and C. Harvey (2009), Investigation of aquifer-estuary interaction using wavelet analysis of fiber-optic temperature data, *Geophys. Res. Lett.*, 36, L06403, doi:10.1029/2008GL036926.
- Henderson, R., F. Day-Lewis, E. Abarca, C. Harvey, H. Karam, L. Liu, and J. Lane (2010), Marine electrical resistivity imaging of submarine groundwater discharge: Sensitivity analysis and application in Waquoit Bay, Massachusetts, USA, *Hydrogeol. J.*, 18, 173–185, doi:10.1007/s10040-009-0498-z
- Johnson, T. C., R. J. Versteeg, A. Ward, F. D. Day-Lewis, and A. Revil (2010), Improved hydrogeophysical characterization and monitoring through parallel modeling and inversion of time-domain resistivity and induced polarization data, *Geophysics*, 75(4), WA27–WA41.
- Kemna, A., A. Binley, F. Day-Lewis, A. Englert, B. Tezkan, J. Vanderborght, and H. Vereecken (2006), Solute and contaminant transport monitoring, in *Applied Hydrogeophysics*, edited by H. Vereecken, 395 pp., NATO Science Series IV: Earth and Environmental Sciences, vol. 71, Springer, Amsterdam.
- Kumar, P. (1997), Wavelet analysis for geophysical applications, *Rev. Geophys.*, 35(4), 385–482.
- Labrecque, D., and X. Yang (2001), Difference inversion of ERT data: A fast inversion method for 3-D in situ monitoring, *J. Environ. Eng. Geophys.*, 6, 83–90.
- Linde, N., J. Doetsch, D. O. G. Jougnot, Y. Dürst, B. Minsley, and J. Luster (2011), Self-potential investigations of a gravel bar in a restored river corridor, *Hydrol. Earth Syst. Sci.*, 15(3), 729–742.
- Mansinha, L., R. Stockwell, and R. Lowe (1997), Pattern analysis with two-dimensional spectral localization: Applications of 2-dimensional S-transforms, *Physica A*, 239, 286–295.
- Mansoor, N., and L. Slater (2007), Aquatic electrical resistivity imaging of shallow-water wetlands, *Geophysics*, 72(5), F211–F221, doi:10.1190/1.2750667.
- McKinley, J. P., C. T. Resch, M. D. Miller, R. M. Kalzuni, V. R. Vermeul, J. V. Moser, and J. M. Zachara (2011), The effects of Columbia River stage on contaminant U concentrations and groundwater compositions at the Hanford 300 Area IFRC, in *Proceedings DOE 6th Annual SBR PI Program Meeting, Rep. PNNL-SA-78391*, U.S. Dep. of Energy, Washington, D.C.
- Nenna, V., A. Pidlisecky, and R. Knight (2011), Application of an extended Kalman filter approach to inversion of time-lapse electrical resistivity imaging data for monitoring infiltration, *Water Resour. Res.*, 47, W10525, doi:10.1029/2010WR010120.
- Nyquist, J., P. Freyer, and L. Toran (2008), Stream bottom resistivity tomography to map ground water discharge, *Ground Water*, 46(4), 561–569, doi:10.1111/j.1745-6584.2008.00432.x.
- Pidlisecky, A., and R. Knight (2011), The use of wavelets and inversion to estimate infiltration rates from electrical resistivity data, *Vadose Zone J.*, 10(2), 697–705, doi:10.2136/vzj2010.0049.
- Selker, J., N. van De Giesen, M. Westhoff, W. Luxemburg, and M. Parlange (2006), Fiber optics opens window on stream dynamics, *Geophys. Res. Lett.*, 33, L24401, doi:10.1029/2006GL027979.
- Singha, K., A. Pidlisecky, F. Day-Lewis, and M. Gooseff (2008), Electrical characterization of non-Fickian transport in groundwater and hyporheic systems, *Water Resour. Res.*, 44, W00D07, doi:10.1029/2008WR007048.
- Sinha, S., P. Routh, and P. Anno (2009), Instantaneous spectral attributes using scales in continuous-wavelet transform, *Geophysics*, 74, 137–142.
- Slater, L., A. Binley, W. Daily, and R. Johnson (2000), Cross-hole electrical imaging of a controlled saline tracer injection, *J. Appl. Geophys.*, 44(2–3), 85–102.
- Slater, L., A. Binley, R. Versteeg, G. Cassiani, R. Birken, and S. Sandberg (2002), A 3D ERT study of solute transport in a large experimental tank, *J. Appl. Geophys.*, 49(4), 211–229.
- Slater, L. D., D. Ntarlagiannis, F. D. Day-Lewis, K. Mwakanyamale, R. J. Versteeg, A. Ward, C. Strickland, C. D. Johnson, and J. W. Lane (2010), Use of electrical imaging and distributed temperature sensing methods to characterize surface water-groundwater exchange regulating uranium transport at the Hanford 300 Area, Washington, *Water Resour. Res.*, 43, W10533, doi:10.1029/2010WR009110.
- Stockwell, R. (1999), S-transform analysis of gravity wave activity from a small scale network of airglow imagers, Ph.D. thesis, Univ. of Western Ontario, Canada.
- Stockwell, R., L. Mansinha, and R. Lowe (1996), Localization of the complex spectrum: The S-transform, *IEEE Trans. Signal Process.*, 44(4), 998–1001.
- Torrence, C., and G. Compo (1998), A practical guide to wavelet analysis, *Bull. Am. Meteorol. Soc.*, 79, 61–78.
- Tsouli, D. (2003), Terrain modeling in forward gravimetric problems: A case study on local terrain effects, *J. Appl. Geophys.*, 54, 145–160.
- Waichler, S., and S. Yabusaki (2005), Flow and transport in the Hanford 300 Area vadose zone-aquifer system, *Rep. PNL-I5125*, 81 pp., Pacific Northwest National Laboratory, Richland, Wash.
- Ward, A., M. Gooseff, and K. Singha (2010), Characterizing hyporheic transport processes—interpretation of electrical geophysical data in coupled stream-hyporheic zone systems during solute tracer studies, *Adv. Water Resour.*, 33(11), 1320–1330, doi:10.1016/j.advwatres.2010.05.008.
- Westinghouse Hanford Company (WHC) (1993), Sampling and analysis of 300-FF-5 operable unit springs and near-shore sediments and river water, *Rep. WHC-SD-EN-TI-125*, Pacific Northwest Laboratory, Richland, Wash.
- Williams, B., C. Brown, W. Um, M. Nimmons, R. Peterson, B. Bjornstadt, and M. Rockhold (2007), Limited field investigation report for uranium contamination in the 300 Area, 300-5 operable unit, Hanford site, Washington, *Rep. PNNL-I6435*, Pacific Northwest National Laboratory, Richland, Wash.